1. Surface area analysis

The BET surface area of the samples was determined from N_2 adsorption/desorption isotherms 77 K (Fig. S1a).Figures S2 b–d present the multipoint BET plots, pore size distribution curves, and comparative surface area bar graphs of the nanocomposites. $NiMnO_3$ exhibits a relatively low BET surface area (25.08 m^2g^{-1}) and pore volume (0.104 cm^3g^{-1}), indicating a dense, weakly porous structure that limits the availability of active sites. In contrast, the BGN nanocomposite shows a significantly enhanced BET surface area (42.30 m^2g^{-1}) and pore volume (0.491 cm^3g^{-1}), along with a larger average pore diameter (12.75 nm), as summarized in Table 1. This increase in surface area and mesoporosity facilitates improved reactant adsorption, electrolyte penetration, and charge accessibility, directly contributing to the enhanced photocatalytic degradation efficiency and electrochemical capacitance. All samples exhibit Type IV (IUPAC) isotherms, confirming their mesoporous nature[1].

Table 1 Surface area and pore volume of BET analysis

Sample	BET surface area(m^2/g)	BJH surface area(m^2/g)	Nitrogen pore volume(cm^3/g)	Pore diameter from BJH (nm)
$NiMnO_3$	25.08	42.76	0.104	3.778
Bi_2O_3/g-C_3N_4/$NiMnO_3$	42.30	65.53	0.491	12.751

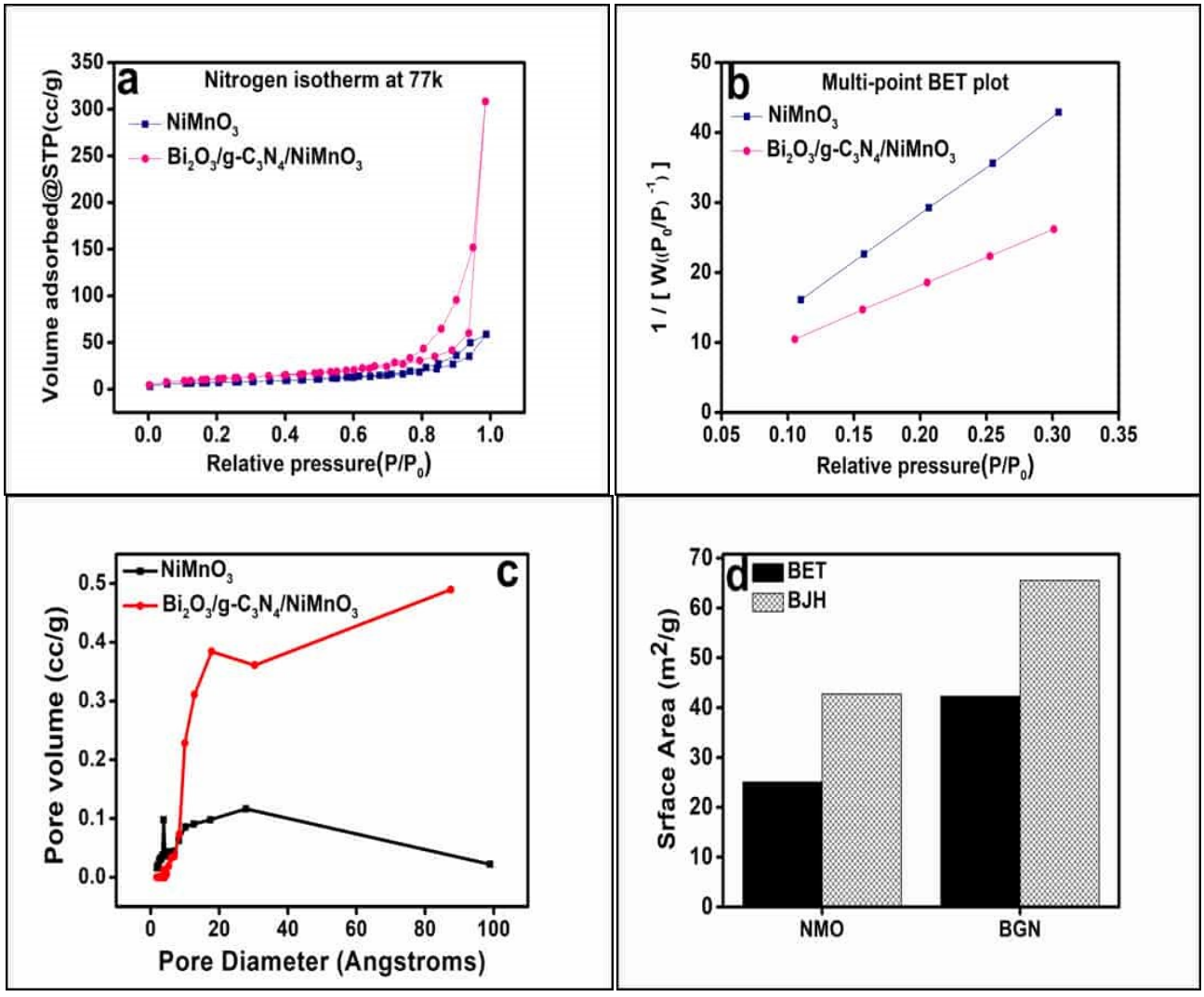

S1. BET surface analysis of $NiMnO_3$ and Bi_2O_3/ g-C_3N_4/ $NiMnO_3$ (BGN) nanocomposite: (a) nitrogen adsorption–desorption isotherms, (b) multi-point BET plot, (c) pore size distribution curves, and (d) bar graph comparison of BET and BJH surface areas.

2. PL and RAMAN

Photoluminescence (PL) spectroscopy was employed to investigate charge-carrier recombination behavior (Fig. S2a). Pristine $NiMnO_3$ exhibits a strong emission peak at 470 nm, indicating a high recombination rate of photogenerated electron–hole pairs[2]. In contrast, the BGN nanocomposite shows a markedly reduced PL intensity at the same wavelength, confirming effective suppression of charge recombination. This PL quenching quantitatively supports improved charge separation efficiency, which correlates well with the observed enhancement in photocatalytic activity and electrochemical performance. Raman spectra (Fig. S2b) display characteristic peaks at 586 and 626 cm^{-1} , corresponding to Ni-O and asymmetric Mn-O stretching modes, respectively, confirming structural integrity and strong metal–oxygen bonding within the composite.[3].

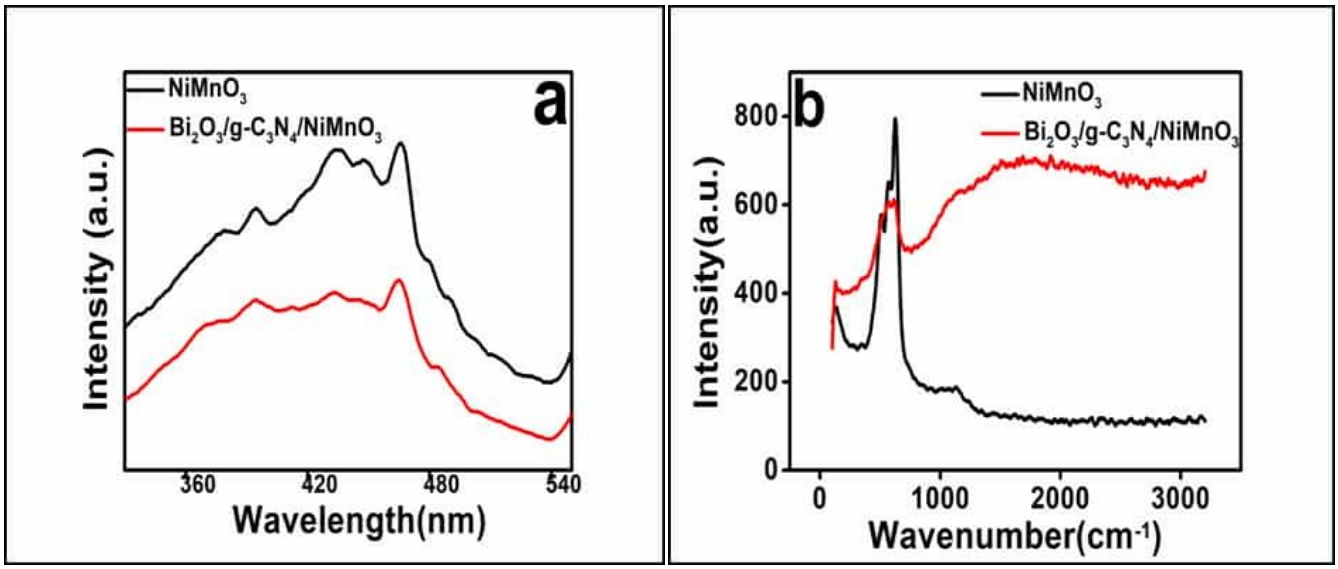

S2. PL(a) and Raman(b) spectra of $NiMnO_3$ and BGN nanocomposites.

3. Degradation of individual dyes

The photocatalytic degradation efficiency of the synthesized photocatalysts was evaluated by monitoring the degradation rates of crystal violet (CV) and congo red (CR) of both dyes under natural sunlight irradiation. The experiments were conducted under standardized conditions: 80 mg of photocatalyst, a reaction temperature of 27 °C or room temperature, a pH 3 for CR due to protonation and acid-catalyzed cleavage of its azo bond, disrupting its chromophore structure, pH 7 for CV because the neutral environment does not protonate or hydrolyze its structure, preserving its chromophore and colour and a neutral pH 6 for mix dyes, as the mildly acidic conditions may slightly protonate Congo red, initiating partial degradation, while Crystal violet largely remains stable due to its resistance to mild pH changes and an initial dye concentration of 40 ppm. Control experiments performed under visible light in the absence of any photocatalyst demonstrated the high photostability of the dyes, as negligible changes in the absorbance of CV and CR dye solution were observed even after 30 minutes of photolysis. To assess the photocatalytic performance under

sunlight irradiation, absorption spectra were recorded for the dye solutions in the presence of various photocatalysts, providing insight into their degradation behaviour.

S3a and S4a demonstrate that the BGN ternary nanocomposites exhibited a gradual decline in removal efficiency for Congo Red (CR) and Crystal Violet (CV) dyes over time. Correspondingly S3b and S4b depict the variation in the dye concentration ratio (C/C_0) with respect to reaction time. Under sunlight exposure, CR and CV dyes showed minimal degradation, with efficiencies of just 6% and 7.2%, respectively. This indicates that both dyes exhibit negligible self-degradation when exposed to sunlight alone. In preliminary dark-phase adsorption tests, equilibrium was reached within 30 minutes for both dyes on various photocatalysts. Upon introducing $NiMnO_3$ nanoparticles, the degradation efficiency significantly improved to 33.1% for CR and 73.7% for CV. Further enhancement was achieved using Bi_2O_3 nanoparticles, with CR and CV degradation rising to 83.1% and 96.4%, respectively, under sunlight. Nevertheless, these values still fell short of ideal performance. Interestingly,integrating g-C_3N_4 nanosheets into the composite markedly improved photocatalytic performance. The ternary BGN system achieved up to 94% and 99% degradation of CR and CV, respectively, within 90 minutes of solar irradiation shown in S3d and S4d.

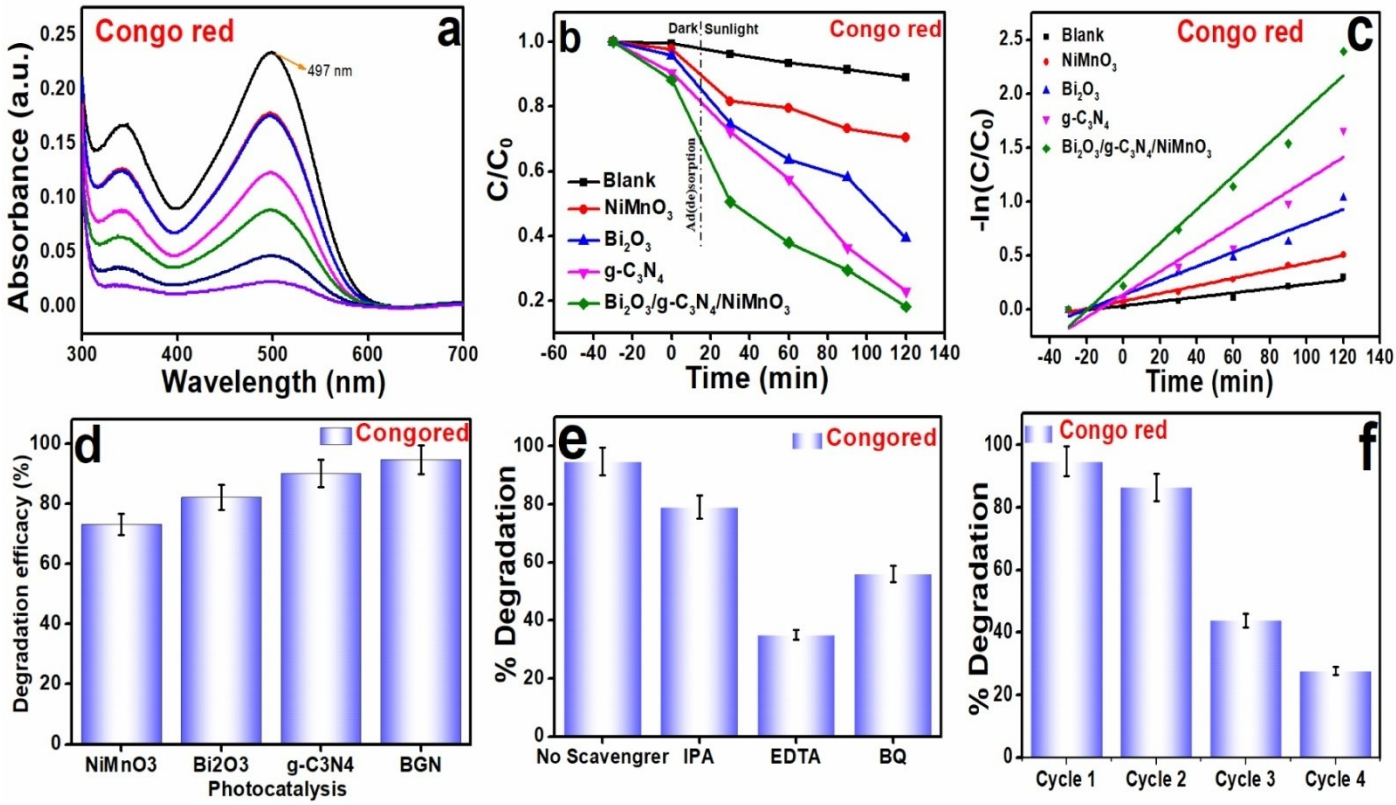

S3. UV–visible absorption analysis of the photocatalytic activity of Bi_2O_3/g-C_3N_4/$NiMnO_3$ ternary nanocomposites: (a) Absorption spectra of congo red dye solution under visible light irradiation, (b) C/C_0 vs. time plot showing dye degradation profile, (c) Pseudo-first-order kinetic fitting, (d) Comparative degradation efficiency, (e) Scavenger experiment identifying key reactive species, and (f) Recyclability assessment over successive photocatalytic cycles.

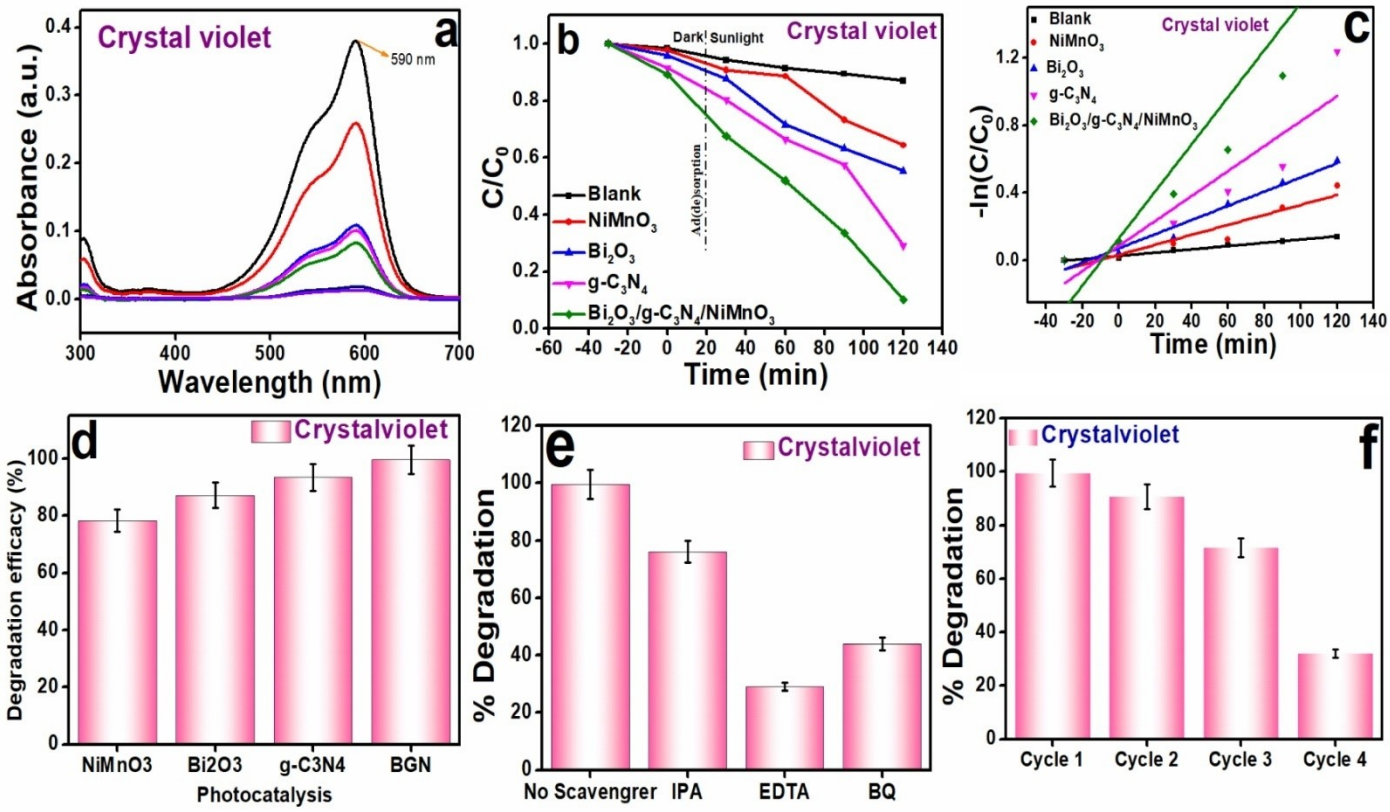

S4. UV–visible absorption analysis of the photocatalytic activity of Bi_2O_3/g-C_3N_4/$NiMnO_3$ ternary nanocomposites for Crystal Violet: (a) Absorption spectra under visible light, (b) C/C_0 vs. time plot, (c) Pseudo-first-order kinetic fit, (d) Degradation efficiency, (e) Scavenger study revealing active species, and (f) Recyclability over multiple cycles.